**Meijie Zhang**
Mem. ASME
Turbomachinery Laboratory,
State Key Laboratory of
Automotive Safety and Energy,
Tsinghua University,
Beijing, 100084, China
e-mail: zhang-mj15@mails.tsinghua.edu.cn

**Xinqian Zheng**[1]
Mem. ASME
Turbomachinery Laboratory,
State Key Laboratory of
Automotive Safety and Energy,
Tsinghua University,
Beijing, 100084, China
e-mail: zhengxq@tsinghua.edu.cn

**Qiangqiang Huang**
Turbomachinery Laboratory,
State Key Laboratory of
Automotive Safety and Energy,
Tsinghua University,
Beijing, 100084, China
e-mail: hqq14@tsinghua.org.cn

**Zhenzhong Sun**
Turbomachinery Laboratory,
State Key Laboratory of
Automotive Safety and Energy,
Tsinghua University,
Beijing, 100084, China
e-mail: sunzz14@mails.tsinghua.edu.cn

# A Novel One-Dimensional–Three-Dimensional Coupled Method to Predict Surge Boundary of Centrifugal Compressors

*Compression systems are widely employed in gas turbine engines, turbocharged engines, and industry compression plants. The stable work of compression systems is an essential precondition for engine performance and safety. A compression system in practice usually consists of upstream and downstream pipes, compressors, plenums and throttles. When a compression system encounters the surge, the flows in the compressor present complex three-dimensional patterns but the flows of other components might present relatively simple one-dimensional patterns. Based on these flow characteristics, this paper proposes a novel simulation method, where one-dimensional and three-dimensional (1D–3D) calculations are coupled, to predict the surge boundary of centrifugal compressors. To validate this method, a high-speed centrifugal compressor is studied both by the proposed 1D–3D coupled method and experimentally. The results show that the differences between the predicted and experimentally determined stable flow range are lower than 5% until the Mach number of blade outlet tip tangential velocity reaches around 1.3. Besides, this method can correctly predict the instantaneous compressor performance during the surge cycle, so it can also be used to explore the surge mechanism and evaluate the blade dynamic force response in the future.* [DOI: 10.1115/1.4042419]

## 1 Introduction

Compression systems where compressors are core components are widely employed in gas turbine engines, turbocharged engines, and industry compression plants [1–3]. The stable work of compression systems is an essential precondition for engine performance and safety. And the biggest threat to the stable work of compression systems is the surge which has remained a significant issue since it is encountered for the first time [4]. Because surge could lead to large mass flow fluctuations in the compressor and cause serious mechanical damage [5,6], accurately obtaining the surge boundary is an indispensable procedure in compressor design and operation.

Various compressor instability models have been developed for the prediction of the flow instability boundary. Koch [7] gave a semi-empirical correlation for the static pressure rise coefficient during axial compressor stall, where the passage geometry, tip clearance, blade row axial space, and Reynolds number were accounted for. In the theoretical and experimental research of compressor surge, Greitzer [8,9] defined a parameter, B, to assess stable operating limits. When this parameter is above a critical value, the mode of compressor instability is surge; while when this parameter is below a critical value, the mode changes to be rotating stall. Based on this theoretical model, Moore and Greitzer [10,11] developed an approximate theory for poststall transients of multistage axial compressor (also called as M-G model), which could describe the growth and decay of a rotating stall cell, and in this study, they also found that the ultimate mode of compressor instability, rotating stall or surge, depended not only on the B parameter but also on the compressor length-to-radius ratio. Subsequently, the lumped parameter model is widely used to study the compressor surge [12,13]. In addition, the experimental results of Longley and Hynes [14] showed that the instability points and stall performance of compressor were properties of the whole compression system rather than a property of the compressor itself, which indicates that the direction of handling the problems about compressor instability must turn to the compression system. Different from previous models where the compressor was replaced by a pure performance characteristic line, a stall inception model consisting of stability eigenvalue equations was developed by Sun et al. [15], and this model could take specific flow patterns and the impeller geometry into account by changing the body force on the impeller.

Except for the theoretical studies, other attempts to solve the prediction of compressor instability are to identify the specific flow fields that are related to compressor flow breakdown by means of three-dimensional simulations and experiments. The simulation of Hoying et al. [16] showed evidence for spike type stall inception for the first time in an axial compressor and revealed the relationship between the tip clearance vortex and stall inception. Vo et al. [17] gave a qualitative criterion, which was that the backflows both at the leading edge and at the trailing edge occurred at the same time, for spike type stall inception in axial compressors based on numerical simulations. Different from the spike type stall inception, März et al. [18] found that the interaction between the tip clearance flow and the incoming flow from the inlet duct, in a low-speed axial compressor, would cause a different vortex, which propagated from the blade suction side to the pressure side but did not spill over to the other flow passage. This phenomenon is called rotating instability, and the compressor

[1]Corresponding author.

Manuscript received June 26, 2018; final manuscript received December 24, 2018; published online February 8, 2019. Assoc. Editor: Riccardo Da Soghe.

could work in a stable mode with the rotating instability, unlike rotating stall. Pullan et al. [19] explained the physical mechanism of spike-type stall inception of axial compressors by the numerical method. They pointed out that the flow separation was caused by high incidence at the leading edge, which could also occur in the zero tip clearance compressor. And the high incidence was the dominant factor in the formation of axial compressor flow instability. The findings of Everitt and Spakovszky [20] on centrifugal compressors supported the conclusion of Pullan et al. [19]. They explored the flow instability in the vaned diffuser by unsteady simulations and experiments, and the results showed that the separation at leading edge near the shroud end-wall moved upstream to the vaneless space due to the reversed pressure gradient, and then, this increased the diffuser inlet blockage which led to flow instability.

There are many instability models for predicting compressor instability boundaries now, but all these models need a given compressor characteristic line or body force distribution on the compressor blades as the input parameters. So when we are designing a new compressor, the capability of these models to predict the instability boundary appears to be limited. Although the results of three-dimensional unsteady simulations in the conditions close to compressor flow instabilities could be influenced by the code employed, the grid, the modeling assumptions, the discretization, etc., it is indeed a promising direction in solving the problem of compressor instabilities. It has been widely used to explore the characteristic flow structures and a series of representative achievements have been obtained, as discussed above. However, the conventional studies by the three-dimensional simulations are always limited to a sole component of compressor and judging whether the compressor is stable or not relies heavily on some characteristic flow structures, which is very qualitative not quantitative. Up to now, accurately predicting the compressor instability boundary is still an unsolved problem. As Day [4] put it, "We can explain what happens when a compressor stalls or surges, but we have little to offer in the way of rigorous rules for designing a more stable compressor."

Surge is related to all the components of compression system including upstream and downstream pipes, compressors, plenums, and throttles. When a compression system encounters the surge, the flows in the compressor present complex three-dimensional patterns but the flows of other components might present relatively simple one-dimensional patterns. Based on these flow characteristics, this work, to the best of our knowledge, is the first time that a novel one-dimensional and three-dimensional (1D–3D) coupled method is proposed to predict the compressor flow instability boundary.

## 2 One-Dimensional–Three-Dimensional Coupled Method

Compressor surge is a system phenomenon. Its onset is related to the flow characteristics of all the components and is greatly influenced by the interactions among them [21]. When the compressor surges, the flows in the compressor present complex three-dimensional characteristics, and the instantaneous compressor performance is very different from that derived from the assumption of steady-state [22]; the flows in the other components of the compression system, including upstream and downstream pipes, plenums, and throttles mainly presented one-dimensional characteristics [23]. (Of course, the flows will present more three-dimensional characteristics if the piping systems are very complex).

According to flow characteristics of different components, this paper established a 1D–3D coupled method, which could capture the corresponding flow characteristics in different components during the surge, and it was applied to a high-speed centrifugal compressor. In this method, the compressor is modeled by a three-dimensional unsteady simulation method to represent the effect of compressor three-dimensional geometry on the surge onset, simulate compressor instantaneous performance, and capture the complex flow structure; the upstream and downstream pipes, the plenum, and the throttle are modeled by a one-dimensional unsteady simulation method (characteristic method) to model the components that are attached to the compressor and the effect of traveling pressure waves on the compressor instantaneous performance. The data exchanges between the three-dimensional model and the one-dimensional model are handled carefully according to different flow directions. In this way, all the flow characteristics in the whole compression system can be modeled reasonably and conveniently, and the costs of time and computation resources still keep at an acceptable level compared with that of a full three-dimensional simulation.

**2.1 One-Dimensional Pipe Flow Simulation.** For the one-dimensional compressible unsteady flow of pipe, the continuity equation in $x$-direction can be written as

$$\frac{\partial \rho}{\partial t} + \rho \frac{\partial v}{\partial x} + v \frac{\partial \rho}{\partial x} + \frac{\rho v}{A} \frac{dA}{dx} = 0 \tag{1}$$

The momentum equation in $x$-direction is

$$\frac{\partial v}{\partial t} + v \frac{\partial v}{\partial x} + \frac{\partial p}{\rho \partial x} + G = 0 \tag{2}$$

In this work, the specific friction force $G$ is defined as [24]

$$G = \frac{4\tau_w}{\rho D} \frac{v}{|v|} = \frac{f v^2}{2D} \frac{v}{|v|} \tag{3}$$

where $f$ is Darcy friction coefficient.

The energy equation is

$$\left(\frac{\partial p}{\partial t} + v \frac{\partial p}{\partial x}\right) - a^2 \left(\frac{\partial \rho}{\partial t} + v \frac{\partial \rho}{\partial x}\right) - (\kappa - 1)\rho(\dot{q} + vG) = 0 \tag{4}$$

where the heat flux $\dot{q} = 0$ in this work.

The advantage of the characteristic method is that it can reduce the partial differential equations to relatively ordinary differential equations [25]. The system of Eqs. (1), (2), and (4) always remains hyperbolic, because all flow conditions studied in this paper are subsonic. So there are three characteristic lines for these equations. The first is to describe the pressure wave which propagates in the same direction as the fluid, which can also be called right-traveling pressure wave

$$\left(\frac{dx}{dt}\right)_R = v + a \tag{5}$$

The second characteristic line is to describe the pressure wave which propagates along the opposite direction to the fluid, which can also be called left-traveling pressure wave

$$\left(\frac{dx}{dt}\right)_L = v - a \tag{6}$$

The third characteristic line is to describe the fluid propagation, which can also be called entropy wave

$$\left(\frac{dx}{dt}\right)_m = v \tag{7}$$

Corresponding to the three characteristic lines, there are three state equations by rearranging the partial differential equations (1)–(3). The state equation of right-traveling pressure wave is

$$a \frac{da_A}{a_A} + \delta R_a + \delta R_f + \delta R_h = d\lambda \tag{8}$$

where $a_A$ is a Riemann invariant that indicates the entropy. The subscript A has no specific meaning but is to be distinguished from the sound speed $a$. $\lambda$ is a Riemann invariant, which is defined by

$$\lambda = a + \frac{\kappa - 1}{2} v \tag{9}$$

$\delta R_a$ represents the effect of variation of pipe area on the right-traveling pressure wave, which is defined by

$$\delta R_a = -\frac{\kappa - 1}{2} \frac{av}{A} \frac{dA}{dx} dt \tag{10}$$

$\delta R_f$ represents the effect of pipe friction on the right-traveling pressure wave, which is defined by

$$\delta R_f = -\frac{\kappa - 1}{2} \left(1 - \frac{\kappa - 1}{a} v\right) G dt \tag{11}$$

$\delta R_h$ represents the effect of pipe heat transfer on the right-traveling pressure wave, which is defined by

$$\delta R_h = \frac{(\kappa - 1)^2}{2a} \dot{q} dt \tag{12}$$

The state equation of left-traveling pressure wave is

$$a \frac{da_A}{a_A} + \delta L_a + \delta L_f + \delta L_h = d\beta \tag{13}$$

where $\beta$ is a Riemann invariant, which is defined by

$$\beta = a - \frac{\kappa - 1}{2} v \tag{14}$$

The physical meanings of $\delta L_a$, $\delta L_f$, and $\delta L_h$ are similar to that of $\delta R_h$, $\delta R_h$, and $\delta R_h$ introduced previously, respectively, which are defined by

$$\delta L_a = \delta R_a \tag{15}$$

$$\delta L_f = \frac{\kappa - 1}{2} \left(1 + \frac{\kappa - 1}{a} v\right) G dt \tag{16}$$

$$\delta L_h = \delta R_h \tag{17}$$

The state equation of entropy wave is

$$\frac{da_A}{a_A} = \frac{\kappa - 1}{2a^2} (\dot{q} + vG) dt \tag{18}$$

Here, the spatial differential equations including four variables $\rho$, $v$, $a$, $p$ have been transformed to solvable ordinary differential equations including three variables $\lambda$, $\beta$, $a_A$.

**2.2 Model of Plenum and Throttle.** For the plenum, assuming that the flow in it is isentropic [26], thus

$$\frac{dp_p}{dt} = \frac{a_p^2}{V_p} (m_{\text{in}} - m_{\text{out}}) \tag{19}$$

where $p_p$ is the static pressure in the plenum; $a_p$ is the sound speed in the plenum; $V_p$ is the volume of plenum; $m_{\text{in}}$ and $m_{\text{out}}$ are the mass flow rates of flow into and out of plenum, respectively.

For the throttle, it is assumed that the pressure difference across the throttle is a function only of the mass flow rate through it [26], thus

$$p_{\text{th}} - p_0 = K_t m_{\text{th}}^2 \tag{20}$$

where $p_{\text{th}}$ is the static pressure before the throttle and $p_{\text{th}} = p_p$, $p_0$ is the atmospheric pressure, $K_t$ is the throttle coefficient, and $m_{\text{th}}$ is the mass flow rate through the throttle and $m_{\text{th}} = m_{\text{out}}$.

**2.3 Method Validation.** Here, the shock tube problem is used to validate this 1D–3D coupled method. The tube is divided up to two parts, as shown in Fig. 1. One part is simulated by the one-dimensional method introduced above, and the other part is simulated by the three-dimensional method. At the beginning $t = 0$ s, the membrane is located 1.2 m from the end of the three-dimensional domain. The pressure of the gas on the right side of the membrane is 300 kPa and that on the left side of the membrane is 100 kPa. The tube is adiabatic, and there is no heat transfer.

The results (the method to get analytical solutions can be found in Ref. [27]) are shown in Fig. 2. The pressure distribution of the 1D–3D coupled simulation result agrees very well with that of the analytical solution, which validates the correctness of the one-dimensional simulation method and the feasibility of the 1D–3D coupled method.

**2.4 Simulation Setup.** ANSYS CFX was employed to calculate the three-dimensional compressor flow. The one-dimensional flows of pipes, plenum, and throttle introduced in Secs. 2.1 and 2.2 were coded in Fortran and compiled into a dynamic library as the user function to exchange data with CFX main program every physical time-step.

The shear stress transport model was chosen for the turbulence closure which has been widely used in the research of turbomachinery [28]. The interfaces of rotor/stator used the transient rotor stator model. The physical time was set to $1 \times 10^{-4}$ s for all the simulations in this paper, because the flow fluctuation frequency

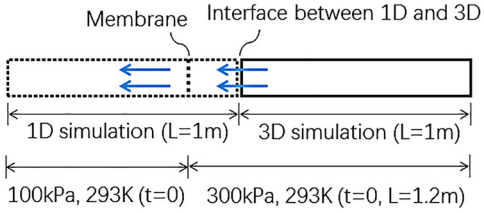


**Fig. 1 Computational model of a shock tube for 1D–3D coupled simulation**

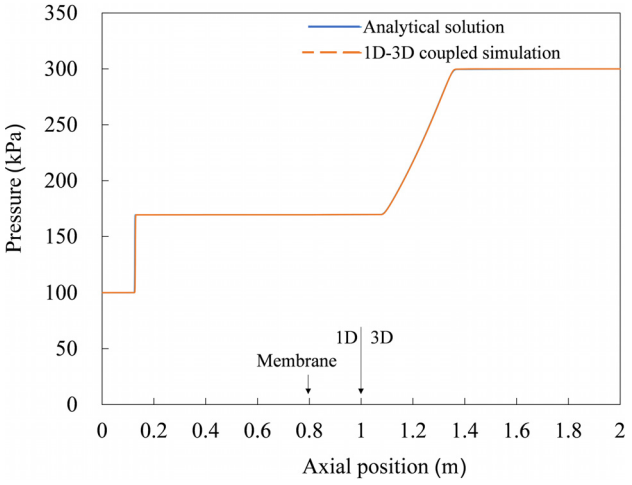


**Fig. 2 Pressure distribution at 1.6 ms for the flow in a shock tube**

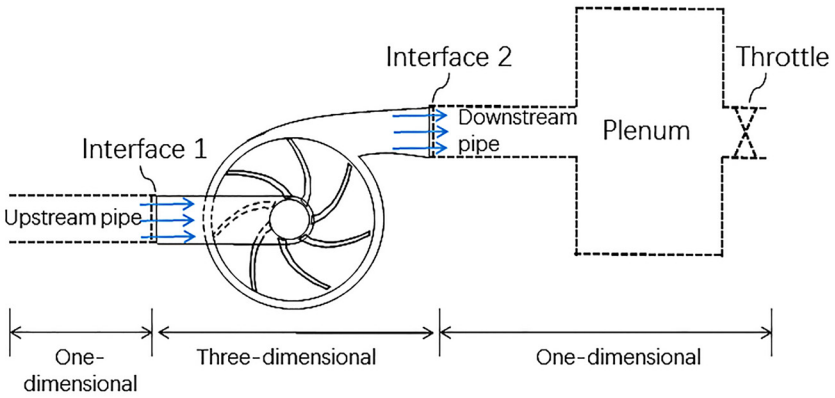


**Fig. 3 The schematic diagram of 1D–3D coupled model**

of surge in centrifugal compressors is usually among 10–20 Hz [29,30], this setup of physical time-step is small enough for capturing the flow characteristics of surge. The inner calculation loop number was set to five which is recommended by CFX solver theory guide [31].

To introduce the boundary conditions, a schematic diagram of 1D–3D coupled model is shown in Fig. 3. With regard to boundary condition, when the flow is normal, from compressor inlet to outlet, total pressure (100,000 Pa) and total temperature (288.15 K) are given as the inlet boundary condition for the upstream pipe; the static pressure which is area-averaged compressor inlet static pressure obtained from calculation results of three-dimensional compressor is given as the outlet boundary condition of the upstream pipe (interface 1 shown in Fig. 3). For the compressor, total pressure and total temperature which are obtained from upstream pipe outlet boundary are given as the compressor inlet boundary condition (interface 1 shown in Fig. 3); static pressure which is obtained from downstream pipe inlet boundary is given as the compressor outlet boundary condition (interface 2 shown in Fig. 3). The compressor inlet and outlet boundaries are both opening which allow the air flows into or out. For the downstream pipe, total pressure and total temperature which are mass-flow-averaged compressor outlet total pressure and total temperature obtained from calculation results of the three-dimensional compressor are given as the inlet boundary condition (interface 2 shown in Fig. 3); static pressure which obtained from the model of plenum and throttle is given as the outlet boundary condition.

While when the flow is reversed, from compressor outlet to inlet, the boundary conditions of components should make some change. For the upstream pipe, the outlet boundary condition becomes total pressure and total temperature. For the compressor, the inlet boundary condition becomes static pressure, and the outlet boundary condition becomes total pressure and total temperature. For the downstream pipe, the inlet and outlet boundary conditions make the same adjustment as the compressor.

## 3 Compressor Geometry and Mesh

The compressor investigated in this paper is a centrifugal compressor with the vaneless diffuser which is used in the turbocharger of a 2.0 L diesel engine. The detail parameters are listed in Table 1.

The three-dimensional computation domain includes an inlet extended pipe (230 mm), an outlet extended pipe (230 mm), full annulus six main blades and six splitter blades with the vaneless diffuser, and a volute, as shown in Fig. 4. The inlet and outlet extended pipes are used to make the inlet and outlet boundary conditions that keep a distance from the compressor inlet and outlet to diminish the nonphysical influence of boundary conditions on the flow fields of compressor.

**Table 1 Detailed compressor parameters**

| Compressor geometry | Value |
|---|---|
| Tip radius at impeller outlet | 25 mm |
| Tip radius at impeller inlet | 18.6 mm |
| Ratio of hub to shroud at impeller inlet | 0.3 |
| Number of blades | 6 + 6 |
| Blade backsweep angle | −38 deg |
| Blade height at impeller outlet | 3.4 mm |
| Vaneless diffuser width | 2.7 mm |
| Area ratio of vaneless diffuser pitch | 0.95 |
| Tip gap at leading edge of main/splitter blade | 0.35 mm |
| Tip gap at trailing edge of main/splitter blade | 0.35 mm |

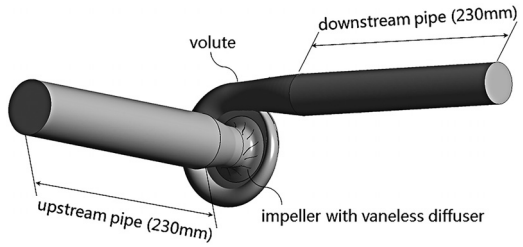


**Fig. 4 Three-dimensional computational domain**

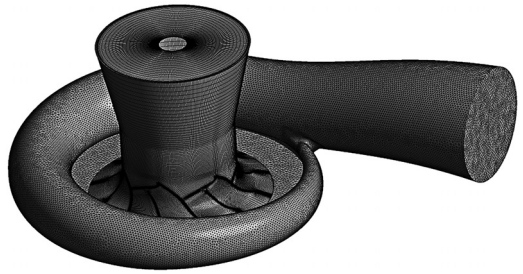

**Fig. 5 Compressor mesh including impeller with vaneless diffuser and volute**

Two different mesh types are adopted in meshing the computational domain. The impeller with vaneless diffuser is meshed by the structure grid. The inlet and outlet extended pipes, and volute are meshed by the unstructured grid in which the prism meshes are used in the boundary layer. The compressor mesh including impeller with vaneless diffuser and volute is shown in Fig. 5. The height of the first mesh layer next to the wall is $1 \times 10^{-4}$ mm.

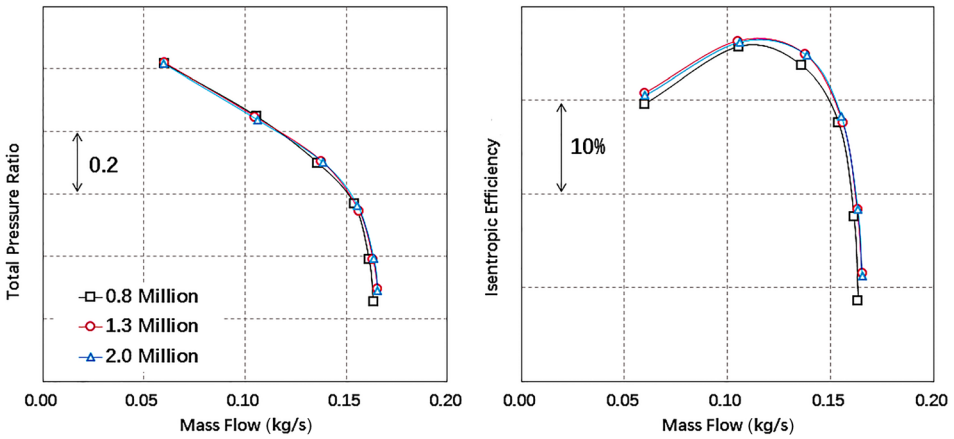


**Fig. 6 Mesh independence study at impeller rotation speed 160,000 rpm**

**Table 2 Mesh information**

| Component | Grid type | Grid number (million) |
|---|---|---|
| Upstream pipe | Unstructured | 1.0 |
| Impeller | Structured | 8.2 |
| Diffuser and volute | Unstructured | 3.2 |
| Downstream pipe | Unstructured | 0.6 |
| The whole domain | — | 13.0 |

**Table 3 Geometry parameter of the other components**

| Other components geometry | Value |
|---|---|
| Upstream pipe diameter | 50 mm |
| Upstream pipe length | 1000 mm |
| Downstream pipe diameter | 37.8 mm |
| Downstream pipe length | 6000 mm |
| Downstream plenum volume | 6700 $m^3$ |

There are 12 mesh layers in the impeller tip clearance. The $Y^+$ is less than 1 in the whole computational domain.

The mesh independence study is conducted on the single passage impeller at rotation speed 160,000 rpm. Three meshes (fine mesh: $2.0 \times 10^6$, moderate mesh: $1.3 \times 10^6$, coarse mesh: $0.8 \times 10^6$) are studied. Figure 6 shows that the results of the moderate mesh and fine mesh are almost the same. So the moderate mesh is adopted in this paper.

The total grid number of the three-dimensional computational domain is around $13 \times 10^6$, and the grid numbers of every component are listed in Table 2.

The geometry parameters of the other components modeled in one dimension are shown in Table 3. In 1D–3D coupled simulations, the parameter determining compressor operation point is throttle coefficient, $K_t$. For a given $K_t$, the compressor outlet boundary condition is derived from the flow of downstream components (downstream pipe, plenum, and throttle).

## 4 Experiment Method and Result

To validate the 1D–3D coupled method, a high-speed small-scale centrifugal compressor is selected in this work. The schematic of the rig is shown in Fig. 7. The length of compressor upstream pipe is 1 m, and the diameter is 50 mm. The length of compressor downstream pipe is 6 m, and the diameter is 37.8 mm. The pressurized air is heated in the combustor, then the high-temperature, high-pressure air expands in the turbine which drives the compressor. The choke mass flow in the experiment is the point of which the efficiency is around 50%. After the choke point, closing the throttle to another smaller mass flow rate point of the compressor and adjusting the fuel flow rate at the same time through the control unit in the experiment rig, to keep a constant compressor shaft speed. Compressor performance characteristics at seven different speed lines from 80,000 rpm to 200,000 rpm are measured by this method. The steady-state sensors of total temperature and total pressure are mounted in the inlet constant pressure chamber and at the compressor outlet, and these steady data are acquired to identify the compressor performance map.

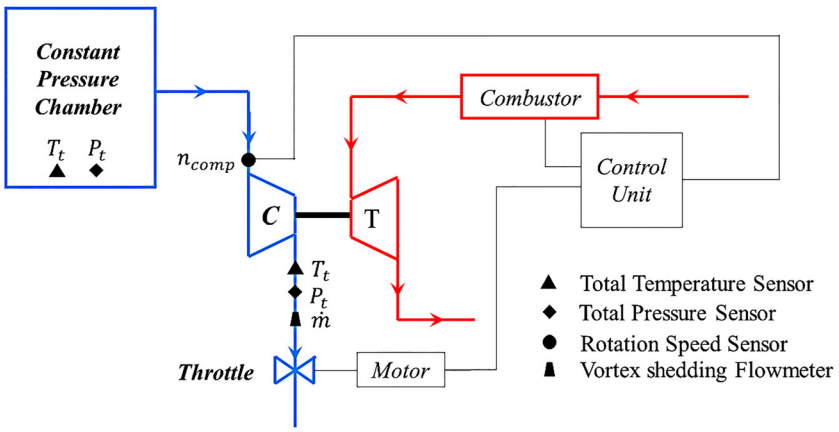


**Fig. 7 Schematic diagram of experiment rig**

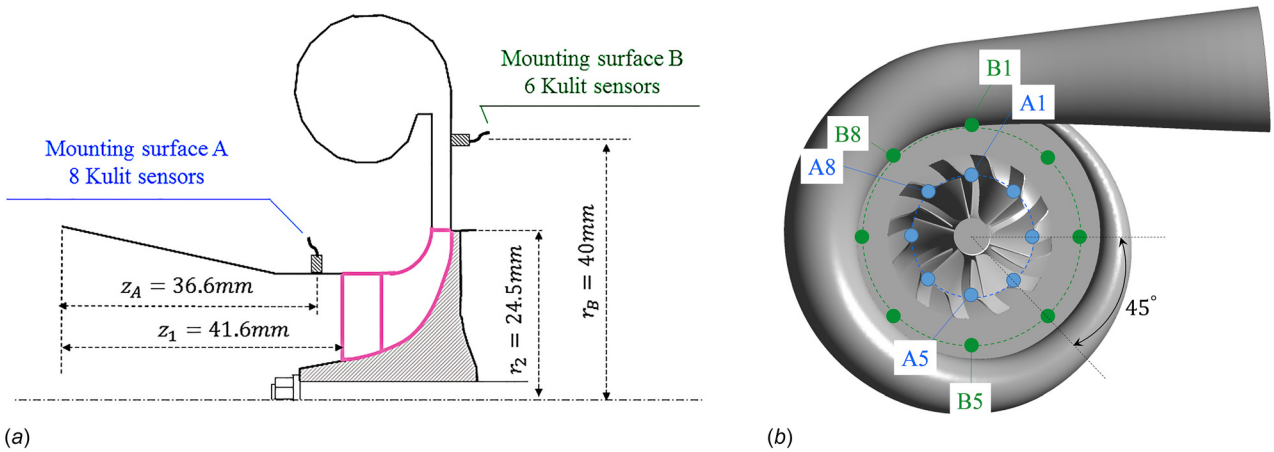


**Fig. 8 Schematic diagram of layout of high-frequency response probes: (*a*) cross section view and (*b*) front view**

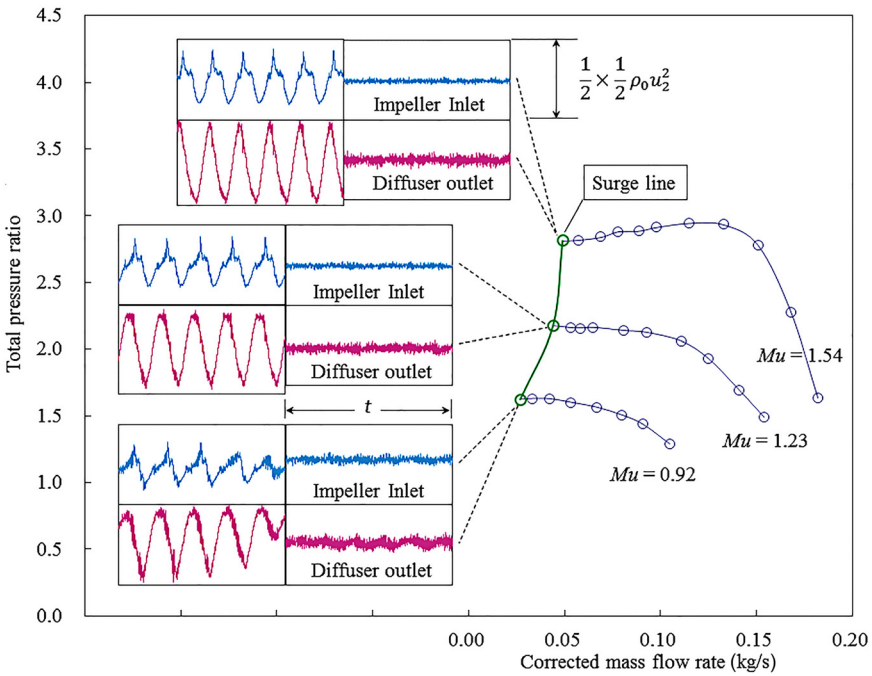


**Fig. 9 Experimental compressor performance**

Except for the steady-state sensors for compressor performance, 16 high-frequency response Kulite static pressure sensors are mounted at two different surfaces which are near compressor inlet and outlet, respectively. The detailed layout is shown in Fig. 8. The dynamic sensors are utilized to monitor the flow field in the compressor at different operation points, especially at the onset of compressor flow instability.

All the signals of dynamic sensors were transmitted to two high-frequency acquisition equipment which are synchronous. The sampling frequency is set to 200 kHz, which is high enough to capture the blade passing frequency (40 kHz) at the maximum rotational speed 200,000 rpm [32,33]. For every operation point, the time to capture dynamic data is more than 10 s, which is to ensure that there is sufficient data for postprocessing. More related information about the experiment rig and measurements can be found in Refs. [29] and [34].

The impeller rotation speed is expressed by a peripheral Mach number, Mu

$$\mathrm{Mu} = \frac{u_2}{\sqrt{kRT_0}} \tag{21}$$

where $u_2$ is impeller outlet tip tangential velocity, and $T_0$ is atmosphere temperature, 288.15 K.

In this work, three typical impeller rotation speed lines are selected to be investigated, where Mu = 0.92, Mu = 1.23, and Mu = 1.54. Figure 9 shows the experimental compressor steady performance and dynamic static pressure evolution of impeller inlet (probe A3) and diffuser outlet (probe B3) near surge points. The surge points are the last stable operation points, and the dynamic static pressure at the impeller inlet and the diffuser outlet is constant. But close the throttle a little further after these last stable operation points, the dynamic static pressure at impeller inlet and diffuser outlet become significantly fluctuating, which can be seen in Fig. 9.

Surge is a low-frequency but high-amplitude flow oscillation phenomenon which can be detected in the whole compression system. The frequency for the single-stage centrifugal compressor is usually about 10–20 Hz (it depends on the compressor size and the pipe systems) [35]. The fluctuation amplitude of static pressure in Fig. 9 is around half of the reference pressure $p_{\mathrm{ref}}$, and the frequency of fluctuation is around 10 Hz, which indicate that the compressor is working in surge [29,30] (of course, there are also

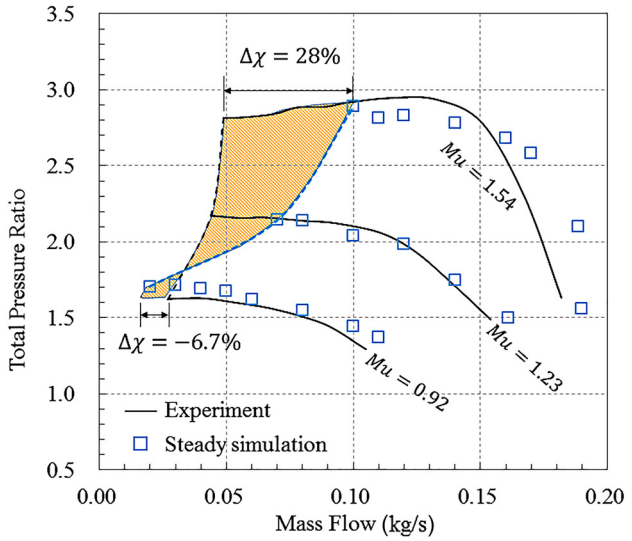


**Fig. 10 Comparison between the steady simulation data and experimental data**

other method to assess the surge points, such as the inlet temperature square deviation variation [32] or the surge severity coefficient variation [36], but the natures of them are the same).

The reference pressure $p_{ref}$ is defined by

$$p_{ref} = \frac{1}{2}\rho_0 u_2^2 \tag{22}$$

where $\rho_0$ is ambient air density, and $u_2$ is the blade tangential speed at impeller outlet tip.

## 5 Surge Boundary Prediction

At first, the steady simulations for compressor performance at three selected typical rotation speed lines are carried out. Then using the stable results of steady simulation as the initial condition, the 1D–3D coupled simulations are conducted by adjusting the throttle coefficient $K_t$ which controls the throttle opening degree to approach the surge boundary.

For boundary conditions of steady simulations, whose computational domain is three-dimensional (Fig. 4), the total pressure (100,000 Pa), total temperature (288.15 K), and turbulence intensity (5%) are given as the inlet boundary condition; the static pressure is given as the outlet boundary condition when the operation point is near the choke, while the mass flow rate is given as the outlet boundary condition for the other operation points which usually can obtain a more extensive flow range for steady simulation. The frozen rotor method is adopted for modeling the rotor and stator interfaces. The stable flow ranges predicted by the steady simulations are always limited by the numerical blowing up. The comparison of stable flow ranges between the steady simulation data and experimental data is shown in Fig. 10.

To quantify the difference of stable flow ranges between the numerical calculations and the experiments, the compressor stable flow range is defined as [37]

$$\chi = \frac{m_{\text{choke, exp}} - m_{\text{surge}}}{m_{\text{choke, exp}}} \times 100\% \tag{23}$$

where $\chi$ is the stable flow range, $m_{\text{choke, exp}}$ is the experiment choke mass flow rate, and $m_{\text{surge}}$ is the surge point mass flow rates of experiment or the last converged point of numerical results.

To obtain the accurate and meaningful difference of surge point between the experiment and numerical results, the experiment choke mass flow rate is used for evaluating the stable flow range of numerical results in Eq. (23). Based on the parameter $\chi$, the $\Delta\chi$

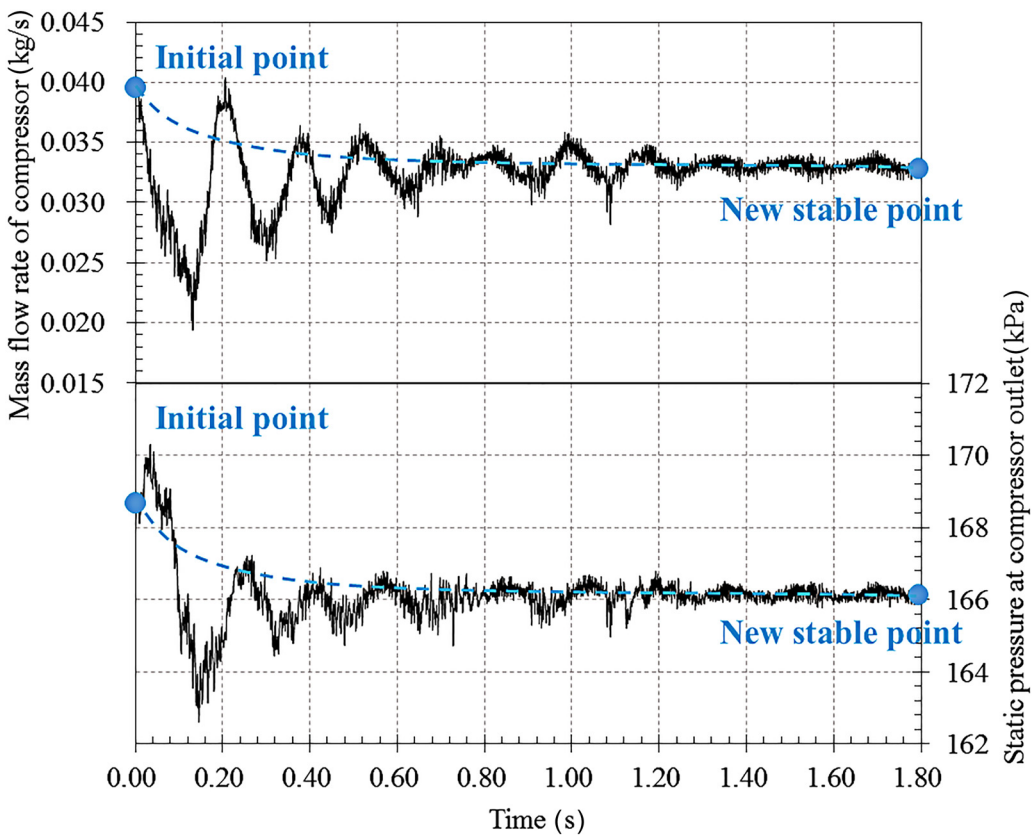


**Fig. 11 Mass flow rate and pressure dynamic response (Kt = $6\times10^7$ kg$^{-1}$m$^{-1}$, Mu = 0.92)**

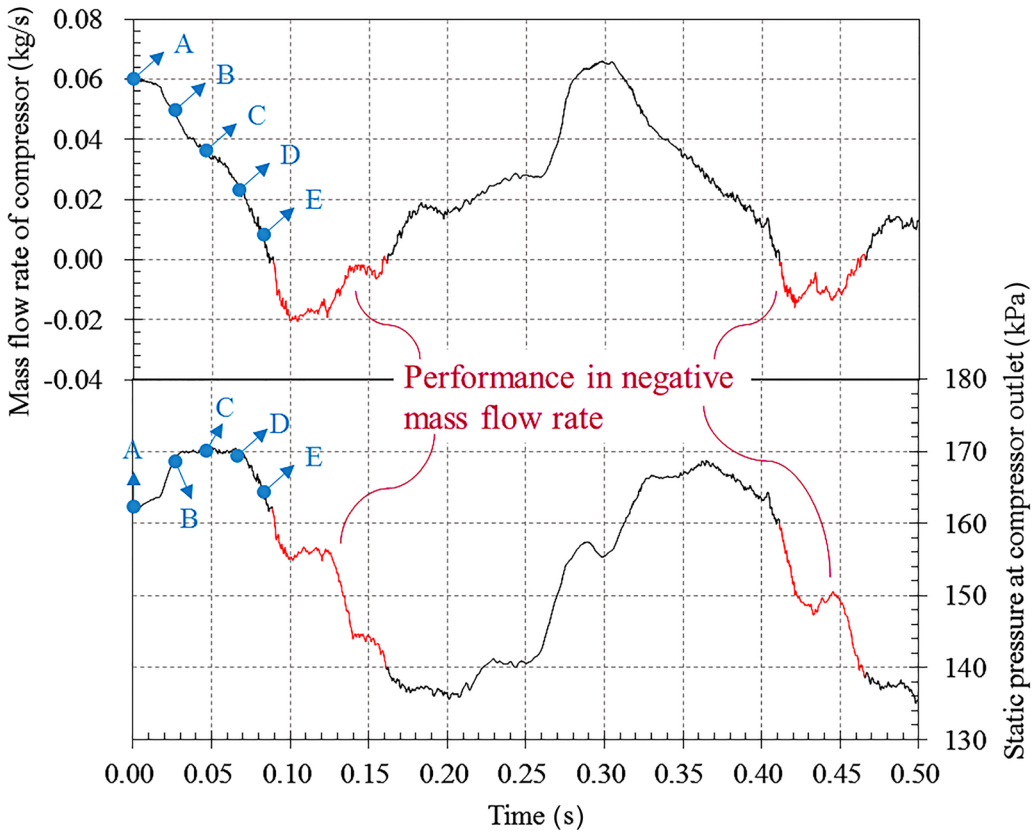


**Fig. 12 Mass flow rate and pressure dynamic response (Kt = $7\times10^7$ kg$^{-1}$m$^{-1}$, Mu = 0.92)**

is used as an evaluation index to illustrate the differences of surge points between the experiment and numerical calculations

$$\Delta\chi_{\text{num}} = \chi_{\text{exp}} - \chi_{\text{num}} \tag{24}$$

As shown in Fig. 10, it can be seen that $\Delta\chi$ increases with the increase of impeller rotation speed and the largest $\Delta\chi$ reaches to 28% when Mu equals to 1.54. The yellow area represents the difference of surge points between the experiment and the steady simulations.

After obtaining the steady simulation results, which can be seen in Fig. 10, the 1D–3D coupled methods are conducted at three different impeller rotation speed lines. The procedure is that conducting 1D–3D coupled simulations with different throttle coefficients Kt to observe the instantaneous performance of the compressor. Taking the case of Mu = 0.92, for example, gradually increase the throttle coefficient (usually several 1D–3D coupled simulations should be tried), according to the steady simulation performance and Eqs. (19) and (20), to find out the critical value, below which the compressor performance is stable but over which the compressor performance goes into a surge cycle. In this case, when throttle coefficient, Kt = $6\times10^7$kg$^{-1}$m$^{-1}$, the compressor can work at a new stable operation point where the mass flow rate and static pressure of compressor can settle on a fixed value. The dynamic responses of mass flow rate and static pressure at compressor outlet are shown in Fig. 11, where the dash line is a simple trend line.

When it is throttled further, Kt = $7\times10^7$kg$^{-1}$m$^{-1}$, the compressor cannot work at a stable operation point any longer and goes into a surge cycle. The dynamic responses of mass flow rate and static pressure at compressor outlet are shown in Fig. 12. The mass flow rate and the static pressure of compressor become fluctuating, and the minimum value of mass flow rate is below zero. It can be seen that at the beginning, with the decrease of mass flow rate, the static pressure at compressor outlet increases, but with the further decrease of mass flow rate, the pressurization capacity of compressor declines and it cannot maintain this high pressure, so the static pressure at compressor outlet drops in succession. This causes the air in the downstream plenum to backflow and even to the negative mass flow rate in the compressor. The results show that the 1D–3D coupling method has more real physical significance in the prediction of compressor surge line; meanwhile, it can present the compressor instability evolution and has a clear criterion to distinguish the stable and the unstable operation point.

The instantaneous performance of compressor at different throttle openings also can be seen clearly in Fig. 13. When the throttle coefficient is small, the compressor can approach a new stable

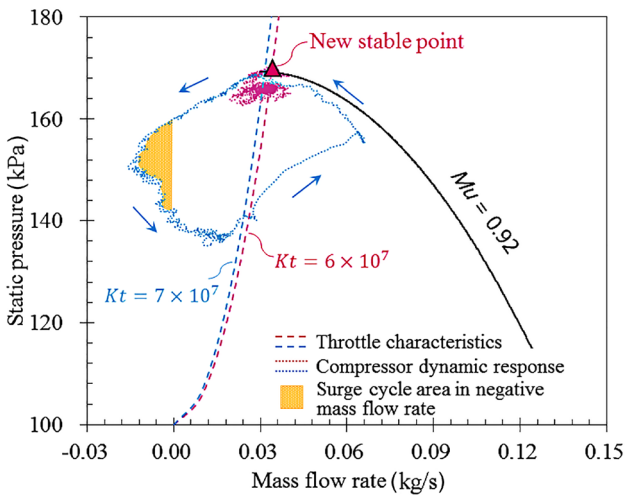


**Fig. 13 Compressor instantaneous characteristics at different throttle openings**

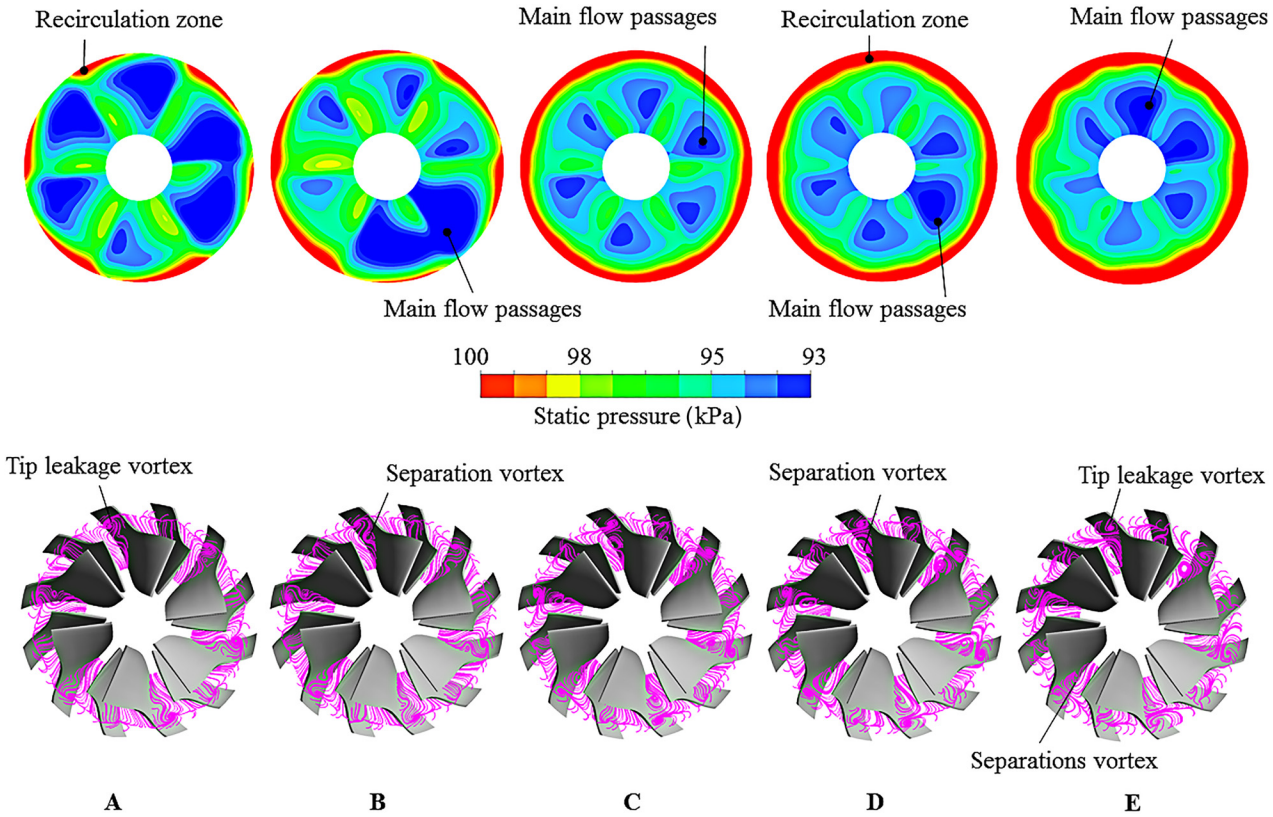


**Fig. 14 Dynamic characteristics of compressor inlet static pressure (top) and flow structures in the passages (bottom)**

point after fluctuations. But increasing the throttle coefficient a little, there is a big switch in the compressor behavior. The compressor suddenly falls into the surge cycle and cannot get a new stable point. The yellow region in Fig. 13 indicates the surge cycle area in the negative mass flow rate. This behavior is similar to the experiment measurements, as shown in Fig. 9, and this also validate the 1D–3D coupled method on the other hand. The appearance of surge cycle is the criterion for predicting the surge boundary by the 1D–3D coupled method. This criterion is more clear compared to that of conventional three-dimensional methods in which judging whether the compressor is stable or not qualitatively relies on some characteristic flow structures. Meanwhile, this criterion is consistent with the physical mechanism of surge, which is very different from the steady simulations of which the criterion depends on the computational converge or blowing-up. Figure 13 vividly demonstrates the significant feature of 1D–3D coupled method in predicting the compressor surge boundary.

When the compressor encounters the surge, the mass flow rate drops suddenly. During this process, five instants are marked in Fig. 12, and the corresponding dynamic characteristics of compressor inlet static pressure and flow structures are shown in Fig. 14. In Fig. 14, the high pressure zones at compressor inlet represent the recirculation, because the recirculation flows are in the stagnation state. The lower the static pressure is, the higher the velocity is, the stronger the flow capacity. At the point A, the recirculation zones are very small, the flow capacities of six main blade passages are approximately the same, and there only exist tip leakage vortexes in the flow passages. As the mass flow rate decreases (points B–E), the recirculation zones extend to the whole circumference and then expand from the blade tip to the hub. Meanwhile, the flow capacities of six passages become uneven, and the main flow passages vary along the circumferential direction. From the standpoint of flow structures, the separation vortexes near main blade suction side appear and increase as the mass flow rate decreases, and then the interaction between the tip leakage vortexes and the separation vortex limits the flow capacity of passages. The time-dependent nature of this interaction leads to the variation of main flow passages along the circumferential direction as discussed above.

The schematic diagram of the two typical flow structures is shown in Fig. 15. When the separation vortex near main blade suction side appears in the blade passage, it will greatly weaken the flow capacity of this passage and even block this passage. Due to the blockage of this passage, the flow incidence of neighboring blade passages will be influenced. The flow incidence of one side

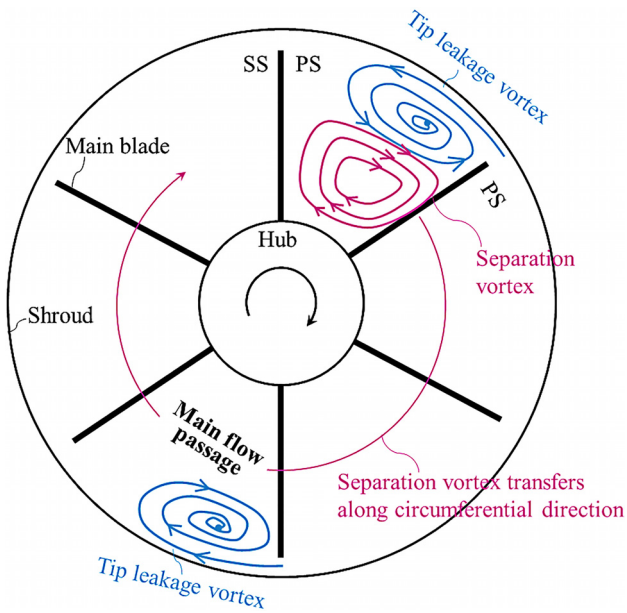


**Fig. 15 Schematic diagram of flow structure in the passage**

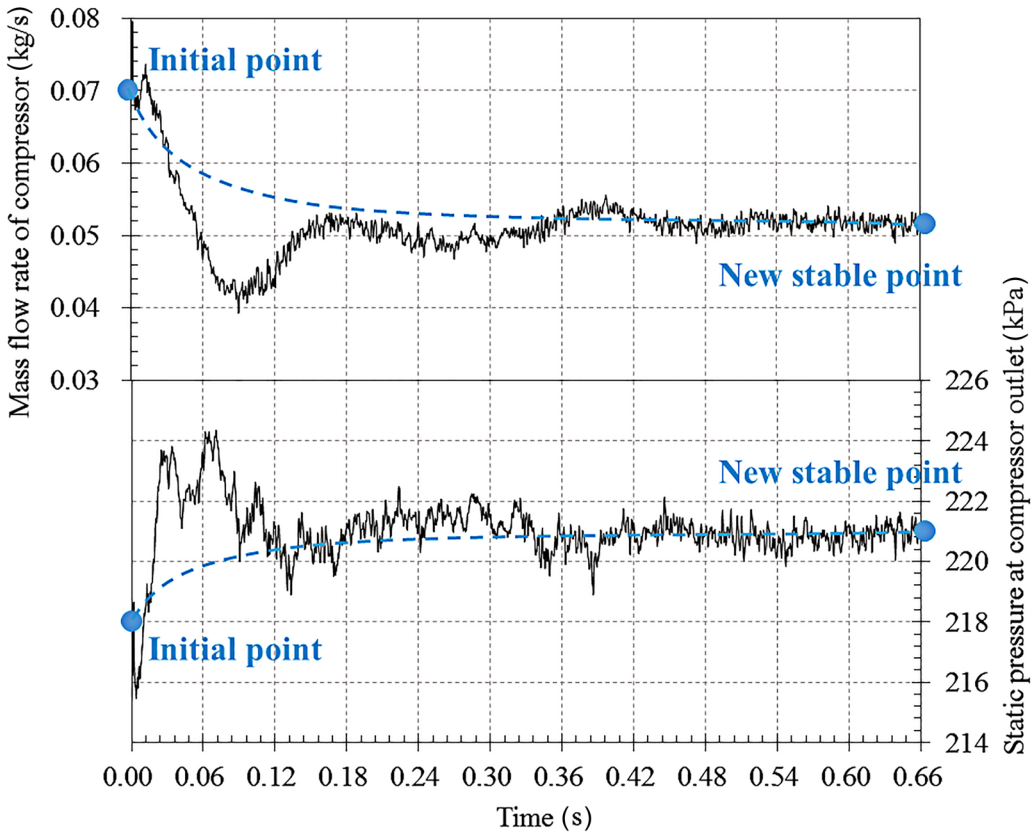


**Fig. 16 Mass flow rate and pressure dynamic response (Kt = $4.5\times10^{7}$ $kg^{-1}m^{-1}$, Mu = 1.23)**

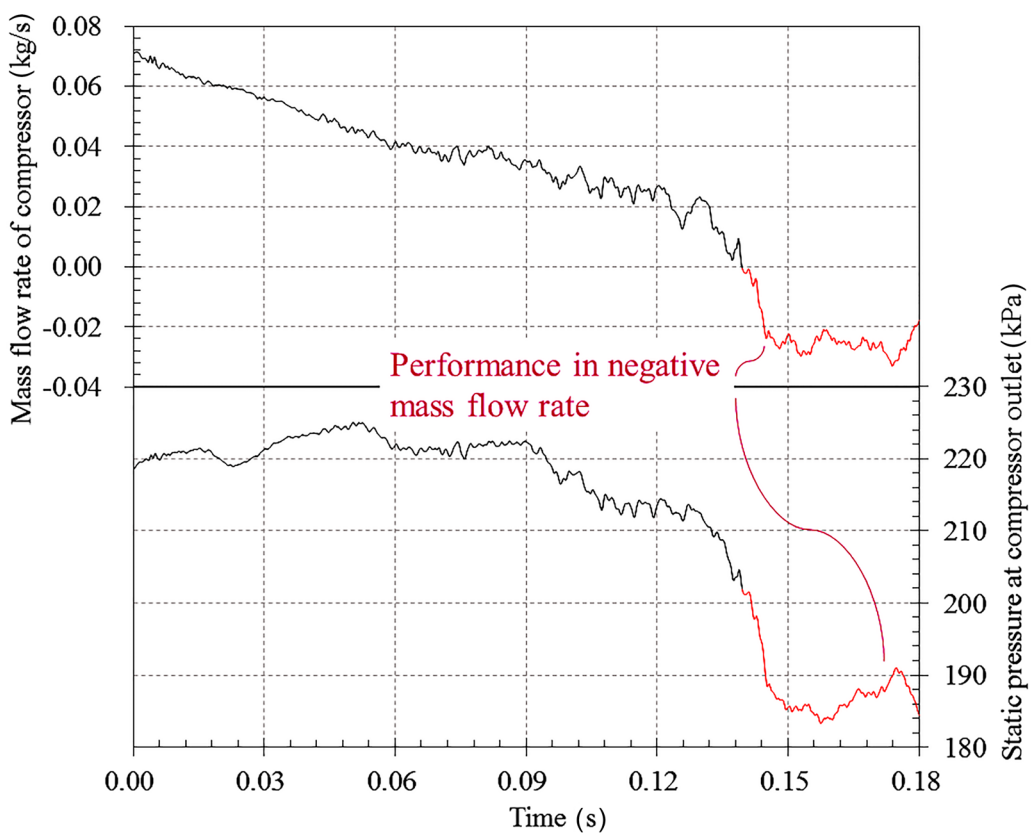


**Fig. 17 Mass flow rate and pressure dynamic response (Kt = $5\times10^{7}$ $kg^{-1}m^{-1}$, Mu = 1.23)**

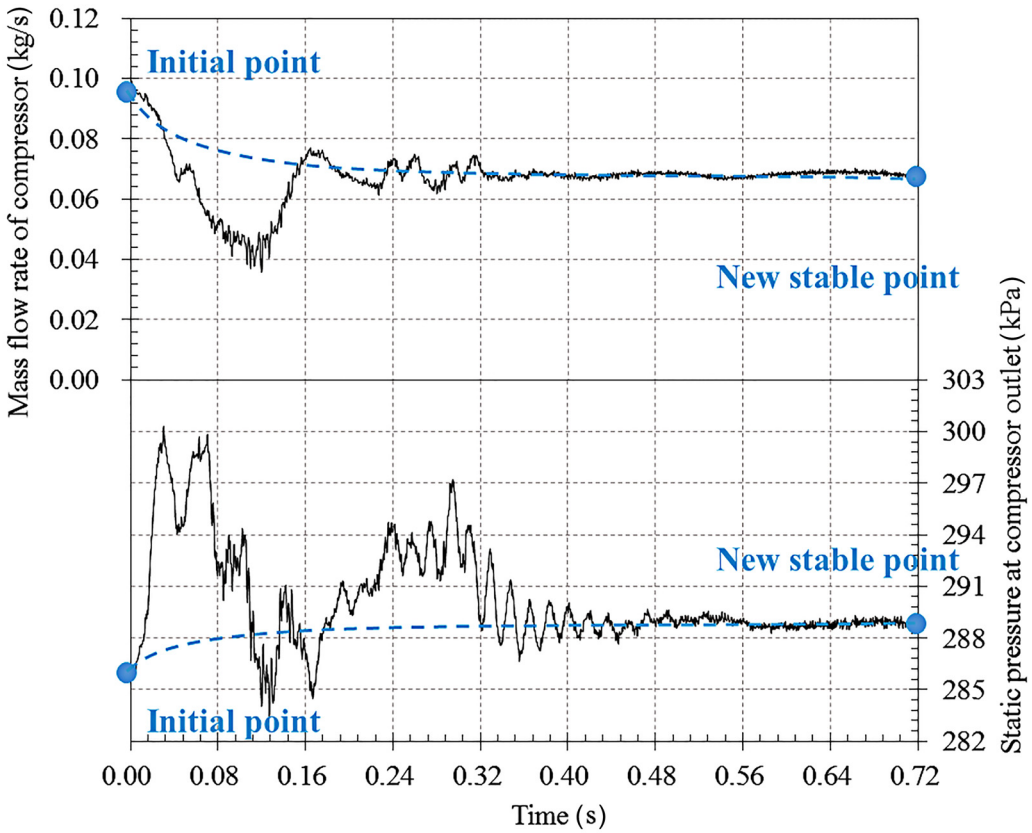


**Fig. 18 Mass flow rate and pressure dynamic response (Kt = $4\times10^7$ kg$^{-1}$m$^{-1}$, Mu = 1.54)**

increases and that of the other side will decrease. Then, the separation vortex will appear in the blade passage of increasing flow incidence, and the separation vortex in the original flow passage is weakened or disappears, i.e., this passage becomes the main flow passage as discussed above. Consequently, the separation vortex transfers along the circumferential direction, so does the main flow passage.

For the impeller rotation speed of Mu = 1.23, setting the solution of last converged point of steady simulation ($m = 0.07$ kg/s) as the initial condition, the results of 1D–3D coupled method show that the compressor can work at a stable operating point when the throttle coefficient is Kt = $4.5 \times 10^7$kg$^{-1}$m$^{-1}$. The dynamic responses of mass flow rate and static pressure at compressor outlet are shown in Fig. 16.

Further throttling, Kt = $5 \times 10^7$kg$^{-1}$m$^{-1}$, the mass flow rate of compressor drops to the negative (Fig. 17), which means that the flow instability occurs in the compressor at this situation and the compressor now goes into surge cycle, as shown in Fig. 13. Considering the computation cost and the intention of this work, there is no time spent to achieve the complete surge cycle, like that of Mu = 0.92.

For the impeller rotation speed of Mu = 1.54, setting the solution of last converged point of steady simulation ($m = 0.1$ kg/s) as the initial condition, the results of 1D–3D coupled method show that the compressor can work at a new stable operating point when the throttle coefficient is Kt = $4 \times 10^7$kg$^{-1}$m$^{-1}$. The dynamic responses of mass flow rate and static pressure at compressor outlet are shown in Fig. 18.

Further throttling, Kt = $5 \times 10^7$kg$^{-1}$m$^{-1}$, the mass flow rate of compressor drops to the negative, and the static pressure at compressor outlet climbs up then decline (Fig. 19). This demonstrates that the flow instability occurs in the compressor at this situation and the compressor now goes into surge cycle, as shown in Fig. 13.

Based on the instantaneous compressor performance discussed above, the surge boundary predicted by 1D–3D coupled method is shown in Fig. 20. The yellow area indicates the difference of surge points between the experiment and 1D–3D coupled method. It can be seen that the surge points are very different from the last converged points of steady simulation (Fig. 10). At the speed of Mu = 0.92, although the steady simulation can converge around mass flow rate of 0.02 kg/s, the results of 1D–3D coupled method indicate that the compressor has gone into the surge cycle at a larger mass flow rate, around 0.03 kg/s. However, at the rotation

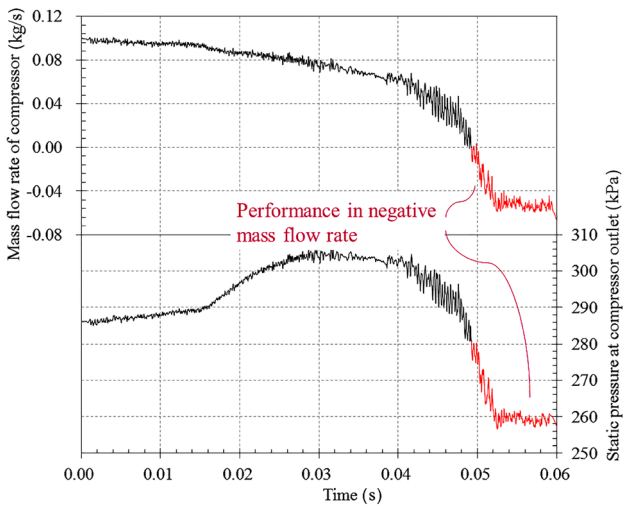


**Fig. 19 Mass flow rate and pressure dynamic response (Kt = $5\times10^7$ kg$^{-1}$m$^{-1}$, Mu = 1.54)**

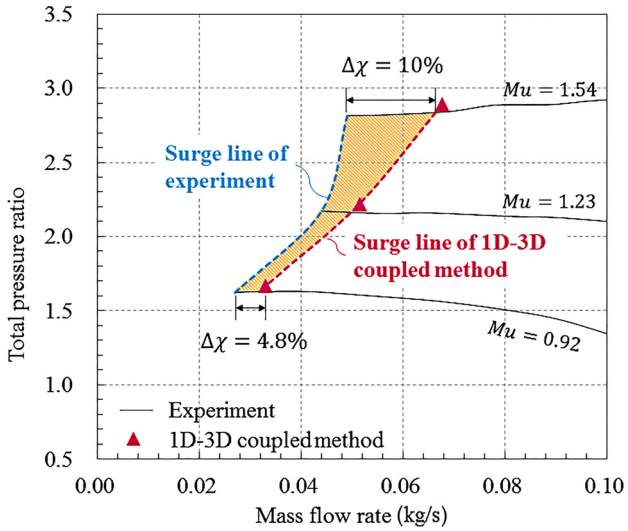


**Fig. 20 Comparison of surge lines between the 1D–3D coupled method and experiment**

**Table 4 Mass flow rate of compressor surge points and comparison of stable flow range**

| | Mu = 0.92 | Mu = 1.23 | Mu = 1.54 |
|---|---|---|---|
| $m_{\text{exp,surge}}$ (kg/s) | 0.027 | 0.044 | 0.049 |
| $m_{\text{std,surge}}$ (kg/s) | 0.020 | 0.070 | 0.100 |
| $m_{\text{1D-3D,surge}}$ (kg/s) | 0.032 | 0.051 | 0.067 |
| $\Delta\chi_{\text{std}}$ (%) | −6.7 | 16.9 | 28.0 |
| $\Delta\chi_{\text{1D-3D}}$ (%) | 4.8 | 4.6 | 10 |

speed of Mu = 1.23 and Mu = 1.54, the surge points predicted by 1D–3D coupled method are at the left side of last converged points of steady simulation.

Comparing the surge line predicted by the 1D–3D coupled method and that of the experiment, the surge line predicted by 1D–3D coupled method is closer to that of the experiment, and the differences of stable flow range are even less than 5% at Mu = 0.92 and Mu = 1.23 (Fig. 20). Although the difference increases to 10% at Mu = 1.54, it is worth noting that the Mu has reached up to 1.54, which is a great challenge for the computational flow dynamics and any progress in this field is strenuous [38].

The steady simulations are not a focused issue, but the results show that there is a vast difference between the surge line of experiment and that of steady simulation, which is a helpful reference for the research of paying close attention to the compressor stable flow range. So at last, the detailed information on the surge points of experiment and numerical results is given in Table 4.

## 6 Conclusion

When surge occurs in the compression system, the flows in the compressor present complex three-dimensional characteristics, and the flows in other components present one-dimensional characteristics. According to these flow characteristics, a novel 1D−3D coupled method is first established to predict the flow instability boundary of compressor. In this method, the compressor is modeled by a three-dimensional unsteady simulation method; the upstream and downstream pipes, the plenum and the throttle are modeled by a one-dimensional unsteady simulation method (characteristic method). In such way, all the typical flow characteristics in the whole compression system are modeled reasonably and conveniently, and the costs of time and computation resources still keep at an acceptable level compared with that of a full three-dimensional simulation.

In the surge boundary prediction, the surge criterion of the 1D–3D coupled method is the appearance of surge cycle. This criterion is more clear compared to that of conventional three-dimensional methods in which judging whether the compressor is stable or not qualitatively relies on some characteristic flow structures. Meanwhile, this criterion is consistent with the physical mechanism of surge, which is very different from that of steady simulations of which the criterion usually depends on the computational converge or blowing-up.

To validate this method, a case of high-speed centrifugal compressor is also studied by dynamic experiment measurements in this work. The results show that the differences of compressor stable flow range between 1D–3D coupled method and the experiment are within 5% until the Mach number of blade outlet tip tangential velocity reaches to around 1.3. This demonstrates that the 1D–3D coupled method is a significantly prospective tool to predict the surge boundary of centrifugal compressors, and the complex flow structure in the compressor also could be explored using this method.

## Funding Data


- National Natural Science Foundation of China (51876097, Funder ID. 10.13039/501100001809).


## Nomenclature

$a$ = speed of sound
$A$ = cross section area of pipe
$a_A$ = the Riemann invariant that indicates entropy
$c_p$ = isobaric heat capacity
$f$ = Darcy friction coefficient
$G$ = specific friction force
$K_t$ = throttle coefficient
$L_a$ = effect of variation of pipe area on the left-traveling pressure wave
$L_f$ = effect of pipe friction on the left-traveling pressure wave
$L_h$ = effect of pipe heat transfer on the left-traveling pressure wave
$m$ = mass flow rate
Ma = Mach number
Mu = Mach number of blade outlet tip tangential velocity
$p$ = pressure
$\dot{q}$ = heat flux
$R$ = ideal gas constant
$R_a$ = effect of variation of pipe area on the right-traveling pressure wave
$R_f$ = effect of pipe friction on the right-traveling pressure wave
$R_h$ = effect of pipe heat transfer on the right-traveling pressure wave
$s$ = entropy
$t$ = time
$T$ = temperature
$u$ = tangential velocity
$v$ = velocity in $x$-direction
$V_p$ = volume of plenum
$x$ = axial position
1D–3D = one-dimensional and three-dimensional
$\beta$ = Riemann invariant on the left-going characteristic line
$\kappa$ = heat capacity ratio
$\lambda$ = Riemann invariant on the right-going characteristic line
$\rho$ = density
$\chi$ = stable flow range

### Subscripts

exp = experiment
in = flow in
$L$ = left-traveling

$m$ = mass flow
num = numerical
out = flow out
$p$ = plenum
$R$ = right-traveling
ref = reference
std = steady simulation
th = throttle
0 = reference parameter
2 = impeller outlet

## References


[1] Munari, E., Morini, M., Pinelli, M., Spina, P. R., and Suman, A., 2016, "Experimental Investigation of Stall and Surge in a Multistage Compressor," ASME J. Eng. Gas Turbines Power, **139**(2), p. 22605.
[2] Da Soghe, R., Bianchini, C., Tommaso Rubino, D., and Toni, L., 2016, "Effects of Impeller Squealer Tip on Centrifugal Compressor Performance," ASME J. Eng. Gas Turbines Power, **139**(3), p. 32603.
[3] Theotokatos, G., and Kyrtatos, N. P., 2016, "Investigation of a Large High-Speed Diesel Engine Transient Behavior Including Compressor," ASME J. Eng. Gas Turbines Power, **125**(2), pp. 580–589.
[4] Day, I. J., 2015, "Stall, Surge, and 75 Years of Research," ASME J. Turbomach., **138**(1), p. 11001.
[5] Brun, K., Simons, S., Kurz, R., Munari, E., and Pinelli, M., 2018, "Measurement and Prediction of Centrifugal Compressor Axial Forces During Surge—Part I: Surge Force Measurements," ASME J. Eng. Gas Turbines Power, **140**(1), p. 12601.
[6] Munari, E., Pinelli, M., Brun, K., Simons, S., and Kurz, R., 2018, "Measurement and Prediction of Centrifugal Compressor Axial Forces During Surge—Part II: Dynamic Surge Model," ASME J. Eng. Gas Turbines Power, **140**(1), p. 12602.
[7] Koch, C. C., 1981, "Stalling Pressure Rise Capability of Axial Flow Compressor Stages," ASME J. Eng. Gas Turbines Power, **103**(4), pp. 645–656.
[8] Greitzer, E. M., 1976, "Surge and Rotating Stall in Axial Flow Compressors—Part II: Experimental Results and Comparison," ASME J. Eng. Power, **98**(2), pp. 199–211.
[9] Greitzer, E. M., 1976, "Surge and Rotating Stall in Axial Flow Compressors—Part I: Theoretical Compression System Model," ASME J. Eng. Power, **98**(2), pp. 190–198.
[10] Moore, F. K., and Greitzer, E. M., 1986, "A Theory of Post-Stall Transients in Axial Compression Systems—Part I: Development of Equations," ASME J. Eng. Gas Turbines Power, **108**(1), pp. 68–76.
[11] Greitzer, E. M., and Moore, F. K., 1986, "A Theory of Post-Stall Transients in Axial Compression Systems—Part II: Application," ASME J. Eng. Gas Turbines Power, **108**(2), pp. 231–239.
[12] Hansen, K. E., Jorgensen, P., and Larsen, P. S., 1981, "Experimental and Theoretical Study of Surge in a Small Centrifugal Compressor," ASME J. Fluids Eng., **103**(3), pp. 391–395.
[13] Hiradate, K., Joukou, S., Sakamoto, K., Shinkawa, Y., and Uchiyama, T., 2016, "Investigation on Pressure Fluctuation Related to Mild Surge in Multistage Centrifugal Blower With Inlet Guide Vane," ASME J. Turbomach., **138**(11), p. 111003.
[14] Longley, J. P., and Hynes, T. P., 1990, "Stability of Flow Through Multistage Axial Compressors," ASME J. Turbomach., **112**(1), pp. 126–132.
[15] Sun, X., Ma, Y., Liu, X., and Sun, D., 2016, "Flow Stability Model of Centrifugal Compressors Based on Eigenvalue Approach," AIAA J., **54**(8), pp. 2361–2376.
[16] Hoying, D. A., Tan, C. S., Vo, H. D., and Greitzer, E. M., 1999, "Role of Blade Passage Flow Structurs in Axial Compressor Rotating Stall Inception," ASME J. Turbomach., **121**(4), p. 735.
[17] Vo, H. D., Tan, C. S., and Greitzer, E. M., 2008, "Criteria for Spike Initiated Rotating Stall," ASME J. Turbomach., **130**(1), p. 11023.
[18] Mäŕz, J., Hah, C., and Neise, W., 2002, "An Experimental and Numerical Investigation Into the Mechanisms of Rotating," ASME J. Turbomach., **124**(3), pp. 367–375.
[19] Pullan, G., Young, A. M., Day, I. J., Greitzer, E. M., and Spakovszky, Z. S., 2015, "Origins and Structure of Spike-Type Rotating Stall," ASME J. Turbomach., **137**(5), p. 51007.
[20] Everitt, J. N., and Spakovszky, Z. S., 2012, "An Investigation of Stall Inception in Centrifugal Compressor Vaned Diffuser," ASME J. Turbomach., **135**(1), p. 11025.
[21] Tamaki, H., 2008, "Effect of Piping Systems on Surge in Centrifugal Compressor," J. Mech. Sci. Technol., **22**(10), pp. 1857–1863.
[22] Spakovszky, Z. S., 2009, "Spike and Modal Stall Inception in an Advanced Turbocharger Centrifugal Compressor 1," ASME J. Turbomach., **131**(7), p. 31012.
[23] Bozza, F., De Bellis, V., Marelli, S., and Capobianco, M., 2011, "1D Simulation and Experimental Analysis of a Turbocharger Compressor for Automotive Engines Under Unsteady Flow Conditions," SAE Int. J. Engines, **4**(1), pp. 1365–1384.
[24] White, F. M., 2008, *Fluid Mechanics*, McGraw-Hill, New York.
[25] Watson, N., and Janota, M. S., 1982, *Turbocharging the Internal Combustion Engine*, The Macmillan Press Ltd, London, UK.
[26] Cumpsty, N. A., 2004, *Compressor Aerodynamics*, Krieger Publishing Company, Malabar, FL.
[27] Anderson, J. D., 2003, *Modern Compressible Flow With Historical Perspective*, McGraw-Hill Higher Education, New York.
[28] Argyropoulos, C. D., and Markatos, N. C., 2015, "Recent Advances on the Numerical Modelling of Turbulent Flows," Appl. Math. Model., **39**(2), pp. 693–732.
[29] Zheng, X., Sun, Z., Kawakubo, T., and Tamaki, H., 2017, "Experimental Investigation of Surge and Stall in a Turbocharger Centrifugal Compressor With a Vaned Diffuser," Exp. Therm. Fluid Sci., **82**, pp. 493–506.
[30] Zheng, X., and Liu, A., 2015, "Phenomenon and Mechanism of Two-Regime-Surge in a Centrifugal Compressor," ASME J. Turbomach., **137**(8), p. 81007.
[31] ANSYS, 2016, "CFX-Solver Theory Guide, ANSYS CFX Release 16.1," ANSYS, Cannosburg, PA.
[32] Liu, A., and Zheng, X., 2013, "Methods of Surge Point Judgment for Compressor Experiments," Exp. Therm. Fluid Sci., **51**, pp. 204–213.
[33] Zheng, X., and Liu, A., 2015, "Experimental Investigation of Surge and Stall in a High-Speed Centrifugal Compressor," J. Propuls. Power, **31**(3), pp. 815–825.
[34] Sun, Z., Zheng, X., and Kawakubo, T., 2018, "Experimental Investigation of Instability Inducement and Mechanism of Centrifugal Compressors With Vaned Diffuser," Appl. Therm. Eng., **133**, pp. 464–471.
[35] De Bellis, V., and Bontempo, R., 2018, "Development and Validation of a 1D Model for Turbocharger Compressors Under Deep-Surge Operation," Energy, **142**, pp. 507–517.
[36] Munari, E., Morini, M., Pinelli, M., Brun, K., Simons, S., and Kurz, R., 2018, "A New Index to Evaluate the Potential Damage of a Surge Event: The Surge Severity Coefficient," ASME Paper No. GT2018-76185.
[37] Zheng, X., and Huang, Q., 2015, "Potential of the Range Extension of Compressors With a Variable Inlet Prewhirl for Automotive Turbocharged Engines With an Ultra-High-Power Density," Proc. Inst. Mech. Eng. Part D, **229**(14), pp. 1959–1968.
[38] Denton, J. D., 2010, "Some Limitations of Turbomachinery CFD," ASME Paper No. GT2010-22540.